

Noise statistics of phase-resolved optical coherence tomography imaging: single- and dual-beam-scan Doppler optical coherence tomography

著者	Makita Shuichi, Jaillon Franck, Jahan Israt, Yasuno Yoshiaki
journal or publication title	Optics Express
volume	22
number	4
page range	4830-4848
year	2014-02
権利	(C) 2014 Optical Society of America. This paper was published in Optics Express and is made available as an electronic reprint with the permission of OSA. The paper can be found at the following URL on the OSA website: http://www.opticsinfobase.org/oe/abstract?uri=oe-22-4-4830 . Systematic or multiple reproduction or distribution to multiple locations via electronic or other means is prohibited and is subject to penalties under law.
URL	http://hdl.handle.net/2241/121254

doi: 10.1364/OE.22.004830

Noise statistics of phase-resolved optical coherence tomography imaging: single- and dual-beam-scan Doppler optical coherence tomography

Shuichi Makita, Franck Jaillon, Israt Jahan, and Yoshiaki Yasuno*

Computational Optics Group in University of Tsukuba,
1-1-1 Tennodai, Tsukuba, Ibaraki 305-8573, Japan

*yasuno@optlab2.bk.tsukuba.ac.jp

<http://optics.bk.tsukuba.ac.jp/COG/>

Abstract: Noise statistics of phase-resolved optical coherence tomography (OCT) imaging are complicated and involve noises of OCT, correlation of signals, and speckles. In this paper, the statistical properties of phase shift between two OCT signals that contain additive random noises and speckle noises are presented. Experimental results obtained with a scattering tissue phantom are in good agreement with theoretical predictions. The performances of the dual-beam method and conventional single-beam method are compared. As expected, phase shift noise in the case of the dual-beam-scan method is less than that for the single-beam method when the transversal sampling step is large.

© 2014 Optical Society of America

OCIS codes: (110.4500) Optical coherence tomography; (120.5050) Phase measurement; (170.3340) Laser Doppler velocimetry; (170.3880) Medical and biological imaging.

References and links

1. Y. Zhao, Z. Chen, C. Saxer, S. Xiang, J. F. d. Boer, and J. S. Nelson, "Phase-resolved optical coherence tomography and optical Doppler tomography for imaging blood flow in human skin with fast scanning speed and high velocity sensitivity," *Opt. Lett.* **25**, 114–116 (2000).
2. B. R. White, M. C. Pierce, N. Nassif, B. Cense, B. H. Park, G. J. Tearney, B. E. Bouma, T. C. Chen, and J. F. d. Boer, "*In vivo* dynamic human retinal blood flow imaging using ultra-high-speed spectral domain optical Doppler tomography," *Opt. Express* **11**, 3490–3497 (2003).
3. R. Leitgeb, L. Schmetterer, W. Drexler, A. Fercher, R. Zawadzki, and T. Bajraszewski, "Real-time assessment of retinal blood flow with ultrafast acquisition by color Doppler Fourier domain optical coherence tomography," *Opt. Express* **11**, 3116–3121 (2003).
4. S. Makita, Y. Hong, M. Yamanari, T. Yatagai, and Y. Yasuno, "Optical coherence angiography," *Opt. Express* **14**, 7821–7840 (2006).
5. B. J. Vakoc, R. M. Lanning, J. A. Tyrrell, T. P. Padera, L. A. Bartlett, T. Stylianopoulos, L. L. Munn, G. J. Tearney, D. Fukumura, R. K. Jain, and B. E. Bouma, "Three-dimensional microscopy of the tumor microenvironment *in vivo* using optical frequency domain imaging," *Nat. Med.* **15**, 1219–1223 (2009).
6. D. Y. Kim, J. Fingler, J. S. Werner, D. M. Schwartz, S. E. Fraser, and R. J. Zawadzki, "*In vivo* volumetric imaging of human retinal circulation with phase-variance optical coherence tomography," *Biomed. Opt. Express* **2**, 1504–1513 (2011).
7. B. Braaf, K. A. Vermeer, V. A. D. Sicam, E. van Zeeburg, J. C. van Meurs, and J. F. de Boer, "Phase-stabilized optical frequency domain imaging at 1-m for the measurement of blood flow in the human choroid," *Opt. Express* **19**, 20886–20903 (2011).

8. R. K. Wang, S. Kirkpatrick, and M. Hinds, "Phase-sensitive optical coherence elastography for mapping tissue microstrains in real time," *Appl. Phys. Lett.* **90**, 164105 (2007).
9. S. G. Adie, X. Liang, B. F. Kennedy, R. John, D. D. Sampson, and S. A. Boppart, "Spectroscopic optical coherence elastography," *Opt. Express* **18**, 25519–25534 (2010).
10. B. F. Kennedy, S. H. Koh, R. A. McLaughlin, K. M. Kennedy, P. R. T. Munro, and D. D. Sampson, "Strain estimation in phase-sensitive optical coherence elastography," *Biomed. Opt. Express* **3**, 1865–1879 (2012).
11. T. Akkin, D. P. Dav, J.-I. Youn, S. A. Telenkov, H. G. R. III, and T. E. Milner, "Imaging tissue response to electrical and photothermal stimulation with nanometer sensitivity," *Lasers Surg. Med.* **33**, 219–225 (2003).
12. S. A. Telenkov, D. P. Dave, S. Sethuraman, T. Akkin, and T. E. Milner, "Differential phase optical coherence probe for depth-resolved detection of photothermal response in tissue," *Phys. Med. Biol.* **49**, 111–119 (2004).
13. D. C. Adler, S.-W. Huang, R. Huber, and J. G. Fujimoto, "Photothermal detection of gold nanoparticles using phase-sensitive optical coherence tomography," *Opt. Express* **16**, 4376–4393 (2008).
14. H. H. Miller, L. Ptaszynski, K. Schlott, C. Debbeler, M. Bever, S. Koinzer, R. Birngruber, R. Brinkmann, and G. Htmann, "Imaging thermal expansion and retinal tissue changes during photocoagulation by high speed OCT," *Biomed. Opt. Express* **3**, 1025–1046 (2012).
15. W. Drexler and J. G. Fujimoto, eds., *Optical Coherence Tomography: Technology and Applications* (Springer, 2008).
16. S. Yazdanfar, C. Yang, M. Sarunic, and J. Izatt, "Frequency estimation precision in Doppler optical coherence tomography using the Cramer-Rao lower bound," *Opt. Express* **13**, 410–416 (2005).
17. B. H. Park, M. C. Pierce, B. Cense, S.-H. Yun, M. Mujat, G. J. Tearney, B. E. Bouma, and J. F. d. Boer, "Real-time fiber-based multi-functional spectral-domain optical coherence tomography at 1.3 μm ," *Opt. Express* **13**, 3931–3944 (2005).
18. B. J. Vakoc, G. J. Tearney, and B. E. Bouma, "Statistical properties of phase-decorrelation in phase-resolved Doppler optical coherence tomography," *IEEE Trans. Med. Imaging* **28**, 814–821 (2009).
19. S. Makita, F. Jaillon, M. Yamanari, M. Miura, and Y. Yasuno, "Comprehensive *in vivo* micro-vascular imaging of the human eye by dual-beam-scan Doppler optical coherence angiography," *Opt. Express* **19**, 1271–1283 (2011).
20. S. Zotter, M. Pircher, T. Torzicky, M. Bonesi, E. Gtzing, R. A. Leitgeb, and C. K. Hitzenberger, "Visualization of microvasculature by dual-beam phase-resolved Doppler optical coherence tomography," *Opt. Express* **19**, 1217–1227 (2011).
21. F. Jaillon, S. Makita, E.-J. Min, B. H. Lee, and Y. Yasuno, "Enhanced imaging of choroidal vasculature by high-penetration and dual-velocity optical coherence angiography," *Biomed. Opt. Express* **2**, 1147–1158 (2011).
22. L. Jong-Sen, K. Hoppel, S. Mango, and A. Miller, "Intensity and phase statistics of multilook polarimetric and interferometric SAR imagery," *IEEE Trans. Geosci. Remote Sens.* **32**, 1017–1028 (1994).
23. R. J. A. Tough, D. Blacknell, and S. Quegan, "A statistical description of polarimetric and interferometric synthetic aperture radar data," *Proc. R. Soc. Lond. A* **449**, 567–589 (1995).
24. J. Walther and E. Koch, "Transverse motion as a source of noise and reduced correlation of the Doppler phase shift in spectral domain OCT," *Opt. Express* **17**, 19698–19713 (2009).
25. V. J. Srinivasan, S. Sakadi, I. Gorczynska, S. Ruvinskaya, W. Wu, J. G. Fujimoto, and D. A. Boas, "Quantitative cerebral blood flow with optical coherence tomography," *Opt. Express* **18**, 2477–2494 (2010).
26. J. Lee, W. Wu, J. Y. Jiang, B. Zhu, and D. A. Boas, "Dynamic light scattering optical coherence tomography," *Opt. Express* **20**, 22262–22277 (2012).
27. A. Szkulmowska, M. Szkulmowski, A. Kowalczyk, and M. Wojtkowski, "Phase-resolved Doppler optical coherence tomography: limitations and improvements," *Opt. Lett.* **33**, 1425–1427 (2008).
28. V. X. Yang, M. L. Gordon, A. Mok, Y. Zhao, Z. Chen, R. S. Cobbold, B. C. Wilson, and I. A. Vitkin, "Improved phase-resolved optical Doppler tomography using Kasai velocity estimator and histogram segmentation," *Opt. Commun.* **208**, 209–214 (2002).
29. A. Moreira, "Improved multilook techniques applied to SAR and SCANSAR imagery," *IEEE Trans. Geosci. Remote Sens.* **29**, 529–534 (1991).
30. J. S. Bendat and A. G. Piersol, *Random Data: Analysis and Measurement Procedures* (John Wiley and Sons, 2010).
31. F. Jaillon, S. Makita, and Y. Yasuno, "Variable velocity range imaging of the choroid with dual-beam optical coherence angiography," *Opt. Express* **20**, 385–396 (2012).
32. S. Makita, F. Jaillon, M. Yamanari, and Y. Yasuno, "Dual-beam-scan Doppler optical coherence angiography for birefringence-artifact-free vasculature imaging," *Opt. Express* **20**, 2681–2692 (2012).
33. K. Kurokawa, K. Sasaki, S. Makita, Y.-J. Hong, and Y. Yasuno, "Three-dimensional retinal and choroidal capillary imaging by power Doppler optical coherence angiography with adaptive optics," *Opt. Express* **20**, 22796–22812 (2012).
34. S. H. Yun, G. J. Tearney, J. F. d. Boer, and B. E. Bouma, "Motion artifacts in optical coherence tomography with frequency-domain ranging," *Opt. Express* **12**, 2977–2998 (2004).
35. I. Grulkowski, I. Gorczynska, M. Szkulmowski, D. Szlag, A. Szkulmowska, R. A. Leitgeb, A. Kowalczyk, and M. Wojtkowski, "Scanning protocols dedicated to smart velocity ranging in spectral OCT," *Opt. Express* **17**, 23736–23754 (2009).

36. L. An, J. Qin, and R. K. Wang, "Ultrahigh sensitive optical microangiography for *in vivo* imaging of microcirculations within human skin tissue beds," *Opt. Express* **18**, 8220–8228 (2010).
37. B. Braaf, K. A. Vermeer, K. V. Vienola, and J. F. de Boer, "Angiography of the retina and the choroid with phase-resolved OCT using interval-optimized backstitched b-scans," *Opt. Express* **20**, 20516–20534 (2012).
-

1. Introduction

Phase-resolved optical coherence tomography (OCT) is a powerful extension to several functional imaging. For example, cross-sectional flow images are obtained by using the Doppler phase shift caused by the motion of blood cells [1–7], the cross-sectional biomechanical property can be mapped by detecting local deformation from the phase of OCT [8–10], and the local photothermal effect can be detected [11–14]. Because these methods are based on the OCT technique [15], they allow three-dimensional high-resolution imaging.

To evaluate the quality of phase-resolved OCT images, a generalized formulation of the phase shift noise would be a powerful technique. Several previous works have addressed the phase shift noise by considering simple additive noise [16] and/or decorrelation of signals because of scanning of a probing beam [17, 18]. However, they lack the contribution of speckle noise; the fluctuation of a signal in a turbid tissue image results in a varying instantaneous signal-to-noise ratio (SNR). Hence, the simple additive noise model with a constant signal intensity is not valid.

Recently, our and other groups introduced the dual-beam-scan Doppler detection method, where two probing beams are separated along the scanning direction, to increase the sensitivity to motion [19–21]. This dual-beam-scan Doppler method measures phase shift between two OCT signals obtained with two probing beams. Because the detection scheme and signal processing of this technique differ from those of conventional phase-resolved OCT, evaluation of its performance is difficult.

In this paper, statistics of phase-resolved OCT imaging with additive, speckle, and decorrelation noises are addressed. The statistics of generalized phase-resolved OCT are formulated in Section 2. The essential parameter is correlation coefficient between two OCT signals and described with specifications of OCT (Section 2.2). The performances of Doppler OCT with conventional single-beam and dual-beam methods are presented in Section 3 according to the formulation in Section 2. We evaluate the performances of phase-resolved Doppler OCT. Phase-resolved imaging performances are compared between the dual-beam-scan and conventional single-beam methods in phantom tissue experiments (Section 4).

2. Statistics of phase-resolved OCT

Here, we describe the statistics of phase-resolved OCT; i.e., phase shift and correlation between two complex OCT signals. Standard deviation of the phase shift is formulated with the support of previous studies in the field of synthetic aperture radar [22, 23]. The population correlation coefficient between two OCT signals is an essential parameter of the statistics of the phase shift. This correlation coefficient is described with specifications of OCT. The statistics of the real estimator of the phase shift are then addressed and a parameter, the effective number of independent samples, is described. Notations of symbols are listed in table 1.

2.1. Statistics of phase shift

The statistics of phase-resolved OCT with additive, speckle, and decorrelation noises are described here. A statistical model with speckle, where the OCT signals vary randomly, is assumed. It is then shown that the effect of additive noise in complex OCT signals can be expressed as a part of decorrelation.

For phase-resolved imaging, the phase shift between two complex OCT signals is used. By considering the two measurements as random variables $\mathbf{G}_1, \mathbf{G}_2$, phase shift is calculated as a

Table 1. List of notations

Symbols	Descriptions
$\Delta\phi_0$	population phase shift between two OCT signals
$\Delta\phi$	realization of phase shift
$\sigma_{\Delta\phi}$	population standard deviation of phase shift
$\sigma_{\Delta\phi_{SS}}$	population standard deviation of phase shift with a static tissue; i.e., noise of phase-resolved flow imaging
$S_{\Delta\phi}$	sample standard deviation of phase shift
$\hat{\Delta\phi}_0$	Maximum likelihood estimation (MLE) of phase shift
ν	number of independent realizations
$\sigma_{\Delta\hat{\phi}_0}$	population standard deviation of phase shift (MLE)
ρ	population correlation coefficient of detected OCT signals
ρ_s	population correlation coefficient of OCT signals
$\rho_{s,SS}$	population correlation coefficient of OCT signals with a static tissue
ρ_{η_1, η_2}	population correlation coefficient of scattering process between two channels
ρ_{h_1, h_2}	population correlation coefficient of point spread functions between two channels
ρ_{g^2}	population correlation coefficient of 2nd order detected OCT signals
$\rho_{g^2, SS}$	population correlation coefficient of 2nd order detected OCT signals with a static tissue
r	sample correlation coefficient
$\hat{\rho}_s$	estimation for correlation coefficient of OCT signals
h	the point spread function of OCT system
SNR	signal-to-noise ratio of OCT system
$ESNR$	representative SNR of two OCT signals
$ENIS$	effective number of independent realizations

phase term of the Hermitian product of two measured OCT signals;

$$\Delta\phi = \arg[g_1^* g_2], \quad (1)$$

where g_1 and g_2 are respectively realizations of \mathbf{G}_1 and \mathbf{G}_2 . Here, the measured OCT signals \mathbf{G}_1 and \mathbf{G}_2 are the sum of complex signals \mathbf{S}_1 and \mathbf{S}_2 and additive noises \mathbf{N}_1 and \mathbf{N}_2 , respectively.

$$\mathbf{G}_1 = \mathbf{S}_1 + \mathbf{N}_1, \quad \mathbf{G}_2 = \mathbf{S}_2 + \mathbf{N}_2. \quad (2)$$

An realization of OCT signal s is the sum of interference signals from scatterers in a coherent detection volume:

$$s = a_R \sum_m a_m \exp[-i2k_c(z_m - z_0)], \quad (3)$$

where a_m is the amplitude of scattered light from the m -th scatterer, and z_m is the axial location of the m -th scatterer. a_R is the amplitude of the reference light, k_c is the central wave number of a broadband light source, and z_0 is the depth at zero delay of the interferometer. By assuming that the scatterers' distribution is random and the density is high compared with resolutions of OCT, the OCT signal is random in space and exhibits fully developed speckle. Hence, \mathbf{S}_1 and \mathbf{S}_2 can be considered as zero-mean complex circular Gaussian variables.

By considering that the additive noises \mathbf{N}_1 and \mathbf{N}_2 are zero-mean complex circular Gaussian variables and independent of each other and the signals \mathbf{S}_1 and \mathbf{S}_2 , the measured signals \mathbf{G}_1 and \mathbf{G}_2 are also zero-mean complex circular Gaussian variables. The statistical properties of the

product of two complex zero-mean circular Gaussian variables have been studied in the field of synthetic aperture radar [22, 23] and it is known that the probability density function (PDF) of the sample phase shift $\Delta\phi$ (Eq. (1)) can be expressed as

$$p_{\Delta\Phi}(\Delta\phi|\rho, \Delta\phi_0) = \frac{1-\rho^2}{2\pi} \left\{ \frac{\beta(\frac{\pi}{2} + \sin^{-1}\beta)}{[1-\beta^2]^{3/2}} + \frac{1}{1-\beta^2} \right\}, \quad (4)$$

where $\beta = \rho \cos(\Delta\phi - \Delta\phi_0)$. Additionally,

$$\rho e^{i\Delta\phi_0} = \frac{E[\mathbf{G}_1^* \mathbf{G}_2]}{\sqrt{E[|\mathbf{G}_1|^2]E[|\mathbf{G}_2|^2]}}, \quad (5)$$

where $E[\cdot]$ is the expectation operator. Equation (5) indicates that the parameters ρ and $\Delta\phi_0$ are the amplitude and phase of the population complex correlation coefficient for the measured signals, respectively. $\Delta\phi_0$ represents the population phase shift.

The expectation and standard deviation of the sample phase shift $\Delta\phi$ are described as

$$E[\Delta\phi] = \frac{\rho \sin \Delta\phi_0}{\sqrt{1-\rho^2 \cos^2 \Delta\phi_0}} \cos^{-1}(\rho \cos \Delta\phi_0), \quad (6)$$

$$\sigma_{\Delta\phi} = \sqrt{\frac{1-\rho^2}{1-\beta'^2} \left[\frac{\pi^2}{4} - \pi \sin^{-1} \beta' + (\sin^{-1} \beta')^2 \right] + \frac{\pi^2}{12} - \frac{\text{Li}_2(\rho^2)}{2}}, \quad (7)$$

where $\beta' = \rho \cos \Delta\phi_0$ and Li_2 is Euler's dilogarithm. The estimators of the expectation and standard deviation are the arithmetic mean and sample standard deviation:

$$\overline{\Delta\phi} = \frac{1}{N} \sum_{n=1}^N \Delta\phi_n, \quad (8)$$

$$S_{\Delta\phi} = \sqrt{\frac{1}{N} \sum_{n=1}^N (\Delta\phi_n - \overline{\Delta\phi})^2}, \quad (9)$$

where N is the number of realizations.

2.2. Correlation coefficient of OCT signals

The correlation coefficient ρ is an essential parameter for defining the statistics of the phase shift. Hence, it determines the performance of phase-resolved OCT. Here, the generalized formulation of correlation coefficient ρ of OCT is described and can be applied to both conventional and dual-beam-scan OCT. The estimations of correlation coefficients are then presented.

The parameter ρ can be described as the following according to the definition of measured signals $\mathbf{G}_1, \mathbf{G}_2$ (Eq. (2));

$$\rho = \frac{\rho_s}{\sqrt{(1+SNR_1^{-1})(1+SNR_2^{-1})}}, \quad (10)$$

where

$$\rho_s = \frac{|E[\mathbf{S}_1^* \mathbf{S}_2]|}{\sqrt{E[|\mathbf{S}_1|^2]E[|\mathbf{S}_2|^2]}}. \quad (11)$$

Equation (11) gives the correlation coefficient between two OCT signals \mathbf{S}_1 and \mathbf{S}_2 and $SNR_i = E[|\mathbf{S}_i|^2]/E[|\mathbf{N}_i|^2]$ ($i=1,2$) are the expected signal-to-noise ratios of each measurement.

As mentioned in the following section (Section 2.2), ρ_s is decreased by means of the displacement of the sampling location on tissue, tissue deformation, scattering, and also, in the case of dual-beam-scan OCT, differences in the system properties between two detections. It can be understood that the denominator of Eq. (10) represents the degree of decorrelation caused by additive random noise. For simplicity, here we define a representative of the SNR as

$$\frac{1}{1 + ESNR^{-1}} \equiv \frac{1}{\sqrt{(1 + SNR_1^{-1})(1 + SNR_2^{-1})}}. \quad (12)$$

Note that the previously presented formula for decorrelation noise of Doppler OCT (Eq. (10) in [18]) is identical to Eq. (4) when $\rho = \alpha^2$: i.e., the correlation coefficient depends only on transversal sampling displacement, and $\Delta\phi_0 = 0$. However, the current model presented here includes the effects of both additive noise and speckle noise. The measured OCT signal \mathbf{G} is assumed to be the sum of the varying signal \mathbf{S} and noise \mathbf{N} . The effect of speckle on phase shift might be accounted for by the varying instantaneous signal-to-noise ratio of each realization $|s|^2/|n|^2$.

The correlation coefficient between two OCT signals ρ_s is defined by referring to previous studies [24–26]. For generalization, two OCT signals are assumed to be detected in two independent channels. Here, the OCT signals (Eq. (3)) can be redescrbed as a time series of two channels;

$$s_1(t_1) = \eta_1 * h_1(\mathbf{r}_1(t_1)), \quad s_2(t_2) = \eta_2 * h_2(\mathbf{r}_2(t_2)). \quad (13)$$

This equation is the convolution (*) of the point spread function (PSF) of each channel $h(\mathbf{r}_L)$ and the complex reflectivity distribution of a sample $\eta(\mathbf{r}_L)$. $\mathbf{r}_L = (x_L, y_L, z_L)$ is the laboratory coordinate. The coordinate \mathbf{r} consists of a lateral location of a probing beam and a depth of the sample from zero delay of the interferometer. \mathbf{r} is a function of time since it will change with beam scanning and motion of objects.

The population correlation coefficient of OCT signals in Eq. (11) and population phase shift $\Delta\phi_0$ can be described from the signal cross-correlation coefficient between realizations s_1, s_2 :

$$\rho_s e^{i\Delta\phi_0} \equiv \rho_{s_1, s_2}(t_1, t_2) = \frac{E[s_1^*(t_1)s_2(t_2)]}{\sqrt{E[|s_1(t_1)|^2]E[|s_2(t_2)|^2]}}. \quad (14)$$

Considering Gaussian beam profiles and a Gaussian coherence function of the light source, PSFs are expressed as

$$h_\chi(x_L, y_L, z_L) \propto e^{-2\frac{x_L^2}{w_\chi^2}} e^{-2\frac{y_L^2}{w_\chi^2}} e^{-\frac{\Delta k^2 z_L^2}{8}} e^{-2ik_\chi(z_L - z_0)} \quad (\chi = 1, 2), \quad (15)$$

where w_χ is the beam spot radius at $1/e^2$ of the χ -th channel. Δk is the full width at $1/e^2$ of a Gaussian spectrum of a light source in unit of wavenumber. Then, the population correlation coefficient of OCT signals ρ_s and population phase shift $\Delta\phi_0$ are obtained by substituting Eq.

(15) and (13) into Eq. (14):

$$\begin{aligned} \rho_s &\approx \rho_{\eta_1, \eta_2} \\ &\times \frac{2w_1 w_2}{w_1^2 + w_2^2} \sqrt{\frac{2\Delta k_1 \Delta k_2}{\Delta k_1^2 + \Delta k_2^2}} \\ &\times e^{-\frac{2x'(t_1, t_2)^2 + y'(t_1, t_2)^2}{w_1^2 + w_2^2}} e^{-\frac{\Delta k_1^2 \Delta k_2^2}{\Delta k_1^2 + \Delta k_2^2} \frac{z'(t_1, t_2)^2}{8}} \\ &\times e^{-\frac{8(k_{c1} - k_{c2})^2}{\Delta k_1^2 + \Delta k_2^2}} \\ &\times e^{-4 \frac{k_{c1}^2 \Delta k_2^2 + k_{c2}^2 \Delta k_1^2}{\Delta k_1^2 + \Delta k_2^2} D(\frac{t_2 + t_1}{2})(t_2 - t_1)}, \end{aligned} \quad (16)$$

$$\Delta\phi_0 \approx -2 \frac{k_{c1} \Delta k_2^2 + k_{c2} \Delta k_1^2}{\Delta k_1^2 + \Delta k_2^2} z'(t_1, t_2), \quad (17)$$

where ρ_{η_1, η_2} denotes the correlation coefficient of the scattering process between two channels and $(x'(t_1, t_2), y'(t_1, t_2), z'(t_1, t_2)) = \mathbf{r}_2(t_2) - \mathbf{r}_1(t_1)$ is the displacement of the sampling point between two channels caused by motions of the sample and/or beam scan. $D(t)$ is the diffusivity at time t owing to the diffusion process. Note that the shift between spectra of the two channels $k_{c1} - k_{c2}$ decreases the correlation coefficient.

In the case of solid tissues (no diffusion and no deformation), the correlation coefficient can be defined as:

$$\rho_{s, SS} \equiv \rho_{\eta_1, \eta_2} |\rho_{h_1, h_2}(\mathbf{r}'(\Delta t))|, \quad (18)$$

where $\mathbf{r}'(\Delta t) = \mathbf{r}_2(t + \Delta t) - \mathbf{r}_1(t)$ and ρ_{h_1, h_2} is the correlation coefficient of PSFs of the two channels:

$$\rho_{h_1, h_2}(\mathbf{r}') = \frac{2w_1 w_2}{w_1^2 + w_2^2} \sqrt{\frac{2\Delta k_1 \Delta k_2}{\Delta k_1^2 + \Delta k_2^2}} e^{-\frac{2x'^2 + y'^2}{w_1^2 + w_2^2}} e^{-\frac{\Delta k_1^2 \Delta k_2^2}{\Delta k_1^2 + \Delta k_2^2} \frac{z'^2}{8}} e^{-\frac{8(k_{c1} - k_{c2})^2}{\Delta k_1^2 + \Delta k_2^2}} e^{-2i \frac{k_{c1} \Delta k_2^2 + k_{c2} \Delta k_1^2}{\Delta k_1^2 + \Delta k_2^2} z'}. \quad (19)$$

The estimation of the parameter ρ is the sample correlation between realizations g_1 and g_2 :

$$r = \frac{|g_1^*(t_1) g_2(t_2)|}{\sqrt{|g_1(t_1)|^2 |g_2(t_2)|^2}}. \quad (20)$$

Because the sample correlation r is a biased estimation for ρ , a large number of realizations are required for accurate estimation.

According to Eq. (10), the correlation coefficient of the OCT signal $\hat{\rho}_s$ can be estimated as

$$\begin{aligned} \hat{\rho}_s &= (1 + E\hat{SNR}^{-1})r \\ &= \frac{|g_1^*(t_1) g_2(t_2)|}{\sqrt{[|g_1(t_1)|^2 - |n_1|^2][|g_2(t_2)|^2 - |n_2|^2]}}, \end{aligned} \quad (21)$$

where $E\hat{SNR}$ is the estimation of the representative SNR (Eq. (12)):

$$1 + E\hat{SNR}^{-1} = \sqrt{\frac{|g_1(t_1)|^2 |g_2(t_2)|^2}{[|g_1(t_1)|^2 - |n_1|^2][|g_2(t_2)|^2 - |n_2|^2]}}. \quad (22)$$

The mean power of noise $\overline{|n_{\chi}|^2}$ will be estimated from the noise floor level of the OCT system without any tissue.

2.3. Maximum likelihood estimation of phase shift

The mean of phase shift $\Delta\phi$ (Eq. (8)) is a biased estimator for $\Delta\phi_0$. According to the expectation (Eq. (6)), the mean estimator results in large offset of the estimation from the population parameter $\Delta\phi_0$ when it is close to the boundaries of phase measurement range [27]. The maximum likelihood estimation (MLE) of parameter $\Delta\phi_0$ will be used for better estimation. The MLE of population phase shift $\Delta\phi_0$ with ν independent realizations $g_1^{(\kappa)}$ and $g_2^{(\kappa)}$ ($\kappa = 1, \dots, \nu$) is [23]

$$\Delta\hat{\phi}_0 = \arg \left[\sum_{\kappa=1}^{\nu} g_1^{(\kappa)*} g_2^{(\kappa)} \right]. \quad (23)$$

The PDF of the MLE for phase shift becomes [22, 23]

$$p_{\Delta\hat{\phi}_0}(\Delta\hat{\phi}_0|\rho, \Delta\phi_0) = \frac{\Gamma(\nu + \frac{1}{2})(1 - \rho^2)^\nu \rho \cos(\Delta\hat{\phi}_0 - \Delta\phi_0)}{2\sqrt{\pi}\Gamma(\nu)[1 - \rho^2 \cos^2(\Delta\hat{\phi}_0 - \Delta\phi_0)]^{\nu+1/2}} + \frac{(1 - \rho^2)^\nu}{2\pi} {}_2F_1\left(\nu, 1; \frac{1}{2}; \rho^2 \cos^2(\Delta\hat{\phi}_0 - \Delta\phi_0)\right), \quad (24)$$

where ${}_2F_1$ is Gauss hypergeometric function.

The phase shift noise of the MLE $\sigma_{\Delta\hat{\phi}_0}$ is characterized by first- and second-order moments $E[\Delta\hat{\phi}_0]$, $E[\Delta\hat{\phi}_0^2]$ as

$$\sigma_{\Delta\hat{\phi}_0} = \sqrt{E[\Delta\hat{\phi}_0^2] - E[\Delta\hat{\phi}_0]^2}. \quad (25)$$

The moments of $\Delta\hat{\phi}_0$ can be numerically calculated using Eq. (24). However, the calculation cost is high. To reduce the computation time, approximations of the moments have been found. The moments of $\Delta\hat{\phi}_0$ can be expressed by the summation of an infinite series as shown in Appendix A. The decrement of the higher-order term from the previous term in the series is from about 10 to more than 90 %. Hence, asymptotic expressions of expectation, variance, and other statistics of $\Delta\hat{\phi}_0$ can be obtained by taking the first several ten terms of the series. Summing up to the ~ 30 -th order provides a good approximation. The only exception is the case when $\nu \rightarrow \infty$ or $\rho \rightarrow 1$, where the summation does not asymptotically converge to the real value. However, it is a rare case in real experiments and can thus be ignored.

2.4. Practical estimators

The MLE of phase shift $\Delta\hat{\phi}_0$ has been shown as Eq. (23). However, in the real case, it is almost impossible to acquire several independent samples for a single location.

Frequently, spatial averaging around the point of interest in an image is applied [4, 28]. The extension of the MLE to a spatial moving average is

$$\Delta\hat{\phi}_0 = \arg \left[\sum_i^I \sum_j^J \sum_l^L g_1^*(x_{1+i}, y_{1+j}, z_{1+l}) g_2(x_{1+i}, y_{1+j}, z_{1+l}) \right], \quad (26)$$

where (I, J, L) is the size of the three-dimensional averaging window. In the averaging window, a tissue should be homogeneous and statistical parameters constant; i.e., the temporal changes between two signals and detection conditions should be equivalent. That means that motion of the sample and scanning speed of the probing beam should be constant and deformation

of objects is equivalent inside the window. The problem is that the realizations, the Hermitian products within a moving window, are not independent of each other. The detection regions of each realization partially overlap owing to the spatial extent of the PSF. Hence, the number of independent realizations is not equal to the number of realizations within the window $v \neq IJL$.

To estimate the moments of the estimated phase shift and the sample correlation coefficient, the effective number of independent samples (ENIS) within an averaging window should be known. Taking the analogy of synthetic aperture radar [29], the ENIS can be defined using the cross-correlation coefficient between Hermitian products as

$$ENIS = \frac{I}{1 + 2 \sum_{i=1}^{I-1} \frac{I-i}{I} \rho_{g_2}^2(i\Delta x, 0, 0)} \frac{J}{1 + 2 \sum_{j=1}^{J-1} \frac{J-j}{J} \rho_{g_2}^2(0, j\Delta y, 0)} \times \frac{L}{1 + 2 \sum_{l=1}^{L-1} \frac{L-l}{L} \rho_{g_2}^2(0, 0, l\Delta z)}, \quad (27)$$

where $(\Delta x, \Delta y, \Delta z)$ is the spatial separation between neighboring pixels in the image along each direction. $\rho_{g_2}(i\Delta x, 0, 0)$ is the correlation coefficient between two Hermitian products with the displacement of i image pixels in the x -direction;

$$\rho_{g_2}(i\Delta x, 0, 0) = \frac{|E[\mathbf{G}_1^*(x_1)\mathbf{G}_2(x_1)\mathbf{G}_1(x_{1+i})\mathbf{G}_2^*(x_{1+i})] - E[\mathbf{G}_1^*(x_1)\mathbf{G}_2(x_1)]E[\mathbf{G}_1(x_{1+i})\mathbf{G}_2^*(x_{1+i})]|}{\sqrt{E[|\mathbf{G}_1^*(x_1)\mathbf{G}_2(x_1) - E[\mathbf{G}_1^*(x_1)\mathbf{G}_2(x_1)]|^2]} \sqrt{E[|\mathbf{G}_1^*(x_{1+i})\mathbf{G}_2(x_{1+i}) - E[\mathbf{G}_1^*(x_{1+i})\mathbf{G}_2(x_{1+i})]|^2]}}. \quad (28)$$

In the case of solid tissues, the correlation coefficient can be described by expanding the fourth-order moment in Eq. (28) [30] and using Eq. (18):

$$\rho_{g_2,SS}(i\Delta x, j\Delta y, l\Delta z) = \frac{1}{(1 + ESNR^{-1})^2} |\rho_{h_1,h_1}^*(i\Delta x, j\Delta y, l\Delta z)\rho_{h_2,h_2}(i\Delta x, j\Delta y, l\Delta z)|, \quad (29)$$

ρ_{h_1,h_1} and ρ_{h_2,h_2} are the auto-correlation coefficients of each channel;

$$|\rho_{h_1,h_1}^*(i\Delta x, j\Delta y, l\Delta z)\rho_{h_2,h_2}(i\Delta x, j\Delta y, l\Delta z)| = e^{-\frac{w_1^2+w_2^2}{w_1^2w_2^2}[(i\Delta x)^2+(j\Delta y)^2]} e^{-\frac{(l\Delta z)^2}{16}(\Delta k_1^2+\Delta k_2^2)}. \quad (30)$$

3. Performance of flow imaging with phase-resolved OCT

Here, the statistical properties of phase-resolved OCT investigated in the previous sections are used to analyze phase-resolved Doppler OCTs. The theoretical performances of conventional phase-resolved Doppler OCT and dual-beam-scan Doppler OCT [19, 20, 31] are investigated. Experimental data are acquired to validate the statistical analysis. The comparison of phase-resolved OCTs is then discussed.

Phase-resolved imaging is a common method for cross-sectional flow imaging by OCT. The phase shift between OCT signals at different time points is caused by axial movements of samples, and expressed as

$$\Delta\phi_{flow} = 2nk_c V \Delta t \cos \theta, \quad (31)$$

where symbols are defined as follows: V , the velocity of moving tissue; θ , Doppler angle; Δt , the time delay between the two time points; and n , the refractive index of the sample.

The sensitivity of flow imaging is defined by the minimum detectable flow in images. This minimum detectable flow can be defined as the velocity corresponding to the random variation of the phase shift for surrounding solid tissue.

$$v_{min} = K \frac{\sigma_{\Delta\phi_{SS}}}{\Delta t}, \quad (32)$$

where $\sigma_{\Delta\phi_{SS}}$ indicates a standard deviation of the spatial distribution of the phase shift for the surrounding solid tissue. $K = 1/2nk_c \cos \theta$ is a factor depending on the tissue and system features. Equation (32) clearly shows that longer time delay and smaller phase shift noise increase the sensitivity of flow imaging. To compare the phase-resolved flow imaging performances of conventional Doppler OCT and dual-beam-scan OCT, phase noise in each method is defined in the following sections.

3.1. Conventional phase-resolved Doppler OCT

Conventional Doppler OCT uses a single probe beam and single detection channel, and applies auto-correlation processing to obtain the phase shift. In this case, $h_1 = h_2$ and $\eta_1 = \eta_2$. Under this condition, the signal correlation coefficient with a static tissue is obtained from Eqs. (18) and (19) as

$$\rho_{s,SS}^{(SB)} = e^{-\frac{x_b'^2 + y_b'^2}{w^2}}, \quad (33)$$

where (x_b', y_b') is the transversal displacement of a probing beam between two measurements. In the case of inter-line Doppler [2], $x_b'^2 + y_b'^2 \rightarrow \Delta x^2$, which is the transversal sampling step between adjacent axial lines.

By substituting Eq. (33) into Eqs. (10) and (29) and using Eqs. (7), (25), and (27) with $\Delta\phi_0 = 0$, the phase shift noise in a static tissue is obtained as

$$\sigma_{\Delta\phi_{SS}}^{(SB)} = \begin{cases} \sigma_{\Delta\phi} \Big|_{\rho = \frac{e^{-\delta x^2}}{1+1/ESNR^{(SB)}}} & (IJL = 1) \\ \sigma_{\Delta\hat{\phi}_0} \Big|_{\rho = \frac{e^{-\delta x^2}}{1+1/ESNR^{(SB)}}, v=ENIS_{I-1,J,L}} & (IJL \geq 2) \end{cases}, \quad (34)$$

where $\delta x = \Delta x/w$ is the fractional sampling step between two adjacent axial lines. Since a single-line-shifted image is used to calculate phase shifts, the window size may be reduced by 1 to maintain the same spatial resolution. Note that the $ESNR$ also affects the $ENIS$ as shown by Eq. (29).

3.2. Dual-beam-scan Doppler OCT

The polarization-multiplexing dual-beam-scan Doppler method detects two OCT signals using different polarization states at the same location of the static tissue [19]. Hence, the signal correlation coefficient with a static tissue can be obtained from Eqs. (18) and (19) as

$$\rho_{s,SS}^{(DB)} = \rho_{Pol.} \frac{2w_1 w_2}{w_1^2 + w_2^2} \sqrt{\frac{2\Delta k_1 \Delta k_2}{\Delta k_1^2 + \Delta k_2^2}} e^{-\frac{8(k_{c1} - k_{c2})^2}{\Delta k_1^2 + \Delta k_2^2}}, \quad (35)$$

where $\rho_{\eta_1, \eta_2} \equiv \rho_{Pol.}$ is the correlation coefficient between the scattering process with two different polarization states of probing beams. It is shown that an increasing difference in the PSFs of the two channels decreases the signal correlation coefficient. The same light source, identical performances of detectors, and the same optical setup for two channels are required to maximize the performance of the dual-beam method. In the ideal case, $\rho_{s,SS}^{(DB)} = \rho_{Pol.}$.

By substituting Eq. (35) into Eqs. (10) and (29) and using Eqs. (7), (25), and (27) with $\Delta\phi_0 = 0$, phase shift noise in a static tissue can be described.

$$\sigma_{\Delta\phi_{SS}}^{(DB)} = \begin{cases} \sigma_{\Delta\phi} \Big|_{\rho = \frac{\rho_{s,SS}^{(DB)}}{1+1/ESNR^{(DB)}}} & (IJL = 1) \\ \sigma_{\Delta\hat{\phi}_0} \Big|_{\rho = \frac{\rho_{s,SS}^{(DB)}}{1+1/ESNR^{(DB)}}, v=ENIS_{I,J,L}} & (IJL \geq 2) \end{cases}. \quad (36)$$

4. Evaluation of phase shift noise

To validate and demonstrate the phase-resolved OCT analysis, an experiment using static tissue was conducted. The behaviors of the phase shift noise in phase-resolved OCT and dual-beam-scan OCT are compared.

4.1. Experimental setup and method

A dual-beam-scan OCT (DB-OCT) system was used for experiments of both single-beam and dual-beam Doppler OCT. The comparison between two different methods is eased by using single system because the conditions and system parameters are identical except the probe beam power. The details of the system were described in a previous work [32]. The ophthalmic lens was removed for tissue phantom imaging. A superluminescent diode with central wavelength of 840 nm and spectral bandwidth of 50 nm was used. Polarization optics (i.e., a Faraday rotator and a quarter waveplate) are introduced to avoid phase retardation due to birefringence of samples. The beam spot radius on tissue was estimated to be 16.5 μm using optical simulation software (ZEMAX, Radiant Zemax, LLC, Redmond, WA). The axial resolution was measured to be about 9.5 μm (full-width at half maximum, -6 dB width) in air. Theoretically, this corresponds to $4 \log 2 / \Delta k_{\text{FWHM}} = 4 \sqrt{2 \log 2} / \Delta k$. In this system, two probing beams are divided from the same light source and pass through common optics in the sample arm. It is thus assumed that $\rho_{s,SS}^{(\text{DB})} \approx \rho_{\text{Pol}}$.

The scattering phantom was made by fixing 1 % soybean oil lipid emulsion (Intralipos®20%, Otsuka Pharmaceutical Factory Inc., Japan) with 10 % porcine gelatin (G2500, Sigma-Aldrich Corp., St. Louis, MO).

Phase-resolved OCT imaging was performed with 256 axial lines/frame and different fractional sampling steps δx from 0.1 to 2.

The conventional single-beam Doppler OCT system can use power of two beams into single probe beam. To emulate the single-beam Doppler method using this DB-OCT system, the two detected OCT signals are summed after a bulk motion correction as

$$g(x_i, z_l) = g_H(x_i, z_l) + g_V(x_i, z_l) \exp[-i\Delta\phi_{\text{ch}}(x_i)], \quad (37)$$

where g_H and g_V are measured OCT signals from the two polarization channels of DB-OCT, and $\Delta\phi_{\text{ch}}(x_i) = \arg[\sum_l g_H^*(x_i, z_l)g_V(x_i, z_l)]$ is the phase difference between two channels at each line estimated by taking the argument of summed Hermitian products along the axial direction [33]. Hence, the *ESNR* of the single-beam method is theoretically twice that of the dual-beam method; $ESNR^{(\text{SB})} = 2ESNR^{(\text{DB})}$. Two signals g_1 and g_2 are assigned as $g_1 \triangleq g_H(x_i, z_l), g_2 \triangleq g_V(x_i, z_l)$ in the case of the dual-beam method and $g_1 \triangleq g(x_i, z_l), g_2 \triangleq g(x_{i+1}, z_l)$ in the case of the single-beam method using Eq. (37). The sample phase differences of the dual-beam and single-beam methods are calculated and analyzed.

4.2. Results

Figure 1 is a cross-sectional OCT image of the scattering phantom. The phase-resolved phantom images with several fractional sampling steps are shown in Fig.2. A part of an image with a constant image depth was assigned as a region of interest (ROI) for analysis as indicated by a yellow box in Fig.1 (256 lines \times 10 pixels). A set of 100 B-scans are acquired and each statistics are measured every B-scan. The final measurements of statistics are averages of 100 realizations.

As expected from Eq. (7), the phase shift noise can be characterized by the correlation coefficient of measured signals ρ . In Fig.3, sample standard deviations of sample phase shift $S_{\Delta\phi}$ of dual-beam and emulated single-beam methods are plotted against the sample correlation r

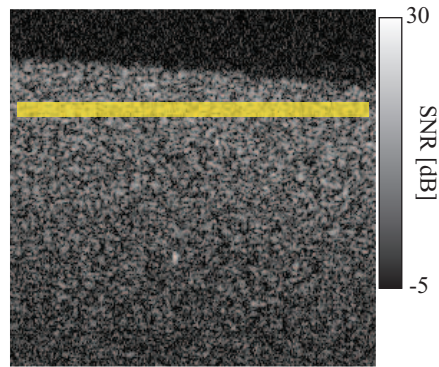


Fig. 1. A cross-sectional OCT image of the tissue phantom. The yellow box indicates the ROI of phase shift analysis.

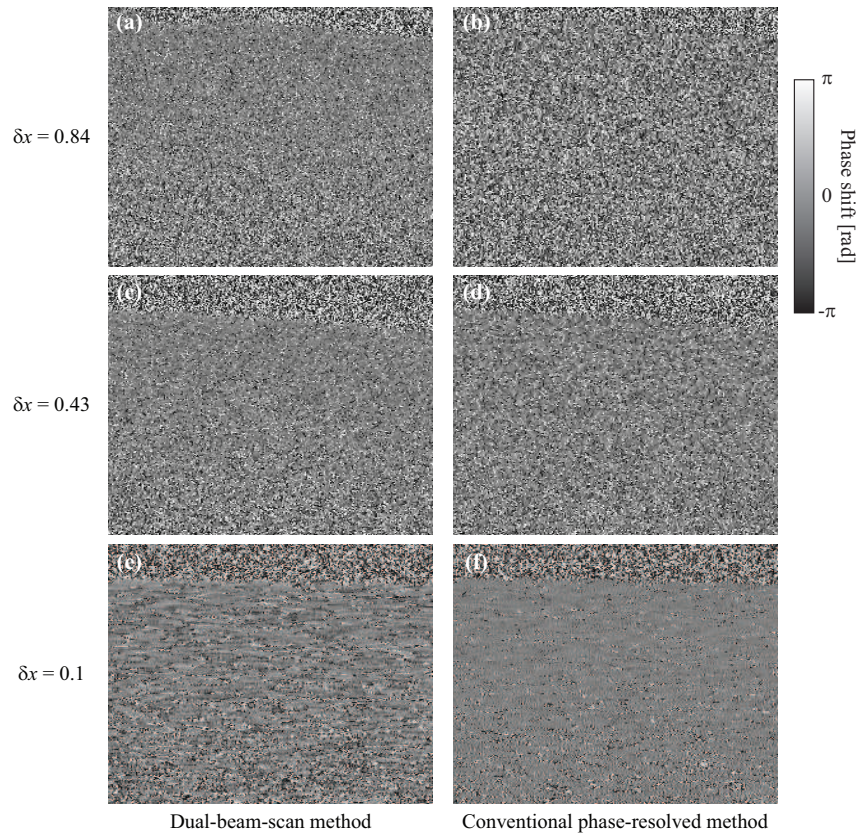


Fig. 2. Phase-resolved images with dual-beam-scan (right column; a, c, e) and emulated conventional phase-resolved (left column; b, d, f) methods. The fractional sampling step was set to be (a), (b) 0.84, (c), (d) 0.43, (e), (f) and 0.1.

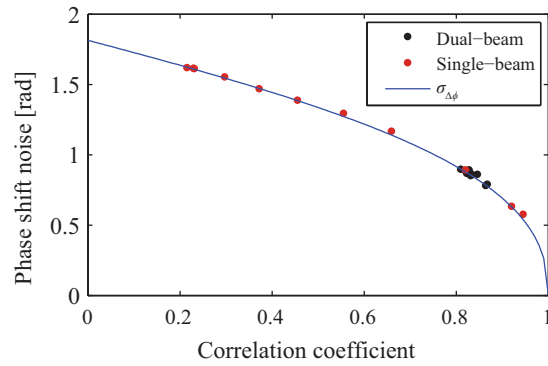


Fig. 3. Scatter plot of phase shift noise vs correlation coefficient. The solid curve shows the population standard deviation of phase shift (Eq. (7)).

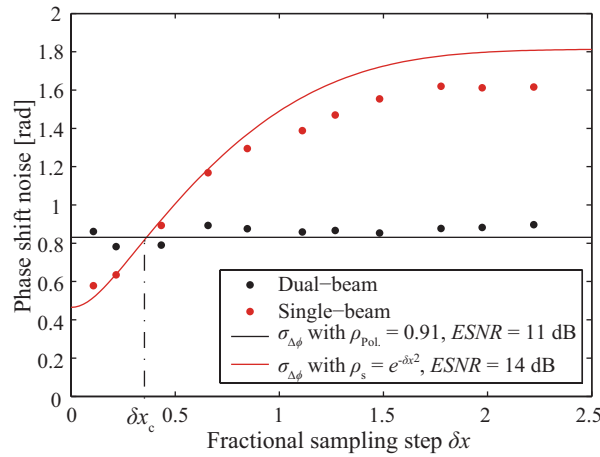


Fig. 4. Phase shift noise vs fractional sampling step δx .

obtained using Eqs. (20) and (9). The solid curve is the line calculated with Eq. (7) at $\Delta\phi_0 = 0$. Experimental and theoretical results are in good agreement.

To compare the dual-beam and single-beam methods, phase shift noise $S_{\Delta\phi}$ is plotted against the fractional sampling step δx in Fig.4. Each curve represents expected phase shift noise (standard deviation of the phase shift, Eq. (7)) for the dual-beam and single-beam methods. The correlation coefficient $\rho_{\text{Pol.}}$ in the dual-beam method was estimated to be 0.91 by averaging the estimation $\rho_{\text{Pol.,}n} = (1 + 1/E\hat{S}\hat{N}R_n^{(\text{DB})})r_n$ of each n -th measurement, where we assume $\rho_s^{(\text{DB})} \approx \rho_{\text{Pol.}}$ and use Eq. (21). $E\hat{S}\hat{N}R^{(\text{DB})}$ is the sample representative SNR of the dual-beam method calculated using Eq. (22) as approx. 11 dB. The population representative SNR $ESNR$ is set to 11 dB for the dual-beam method and 14 dB for the single-beam method. As expected, phase shift noise is almost constant for all fractional sampling steps in the dual-beam method, because two signals are obtained at the same position on the sample no matter the magnitude of the fractional sampling step. The phase shift noise is significantly small compared with that for the single-beam method at large δx . The transitional point of the fractional sampling step where the magnitudes of phase shift noise become identical between single-beam and dual-

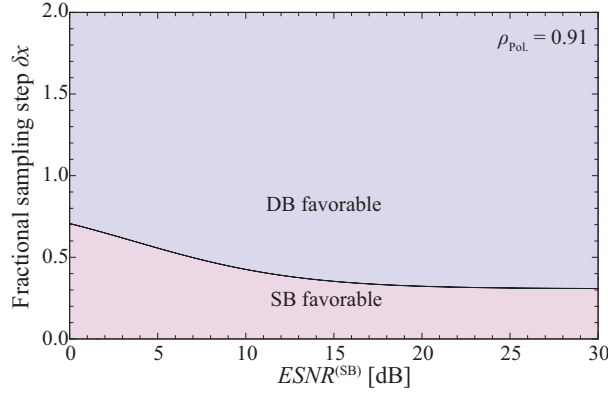


Fig. 5. The transitional point δx_c (Eq. (38)) is plotted. In the upper region, the dual-beam method exhibits less phase shift noise than that of the single-beam method.

beam methods is

$$\begin{aligned} \delta x_c &= \sqrt{-\ln \left[\rho_{\text{Pol.}} \frac{ESNR^{(\text{DB})} ESNR^{(\text{SB})} + 1}{ESNR^{(\text{SB})} ESNR^{(\text{DB})} + 1} \right]} \\ &= \sqrt{-\ln \left[\rho_{\text{Pol.}} \frac{ESNR^{(\text{SB})} + 1}{ESNR^{(\text{SB})} + 2} \right]}. \end{aligned} \quad (38)$$

If the fractional step is larger than this δx_c , the dual-beam method provides superior performance in terms of phase noise compared with the conventional single-beam method.

This is plotted as Fig.5 for $\rho_{\text{Pol.}} = 0.91$. When the fractional sampling step is larger than δx_c , the dual-beam method exhibits less phase shift noise. When $\delta x < \delta x_c$, the single-beam method is better. And δx_c is larger as $ESNR$ decreases. These characteristics can be easily understood as follows. In the case of smaller δx_c and lower $ESNR$, phase shift noise caused by additive random noise is dominant. Since the single-beam method exhibits a larger SNR by a factor of 2, the phase shift noise of the single-beam method is less than that of the dual-beam method.

In Fig.4, the predicted phase shift noise is greater than the experimental results at large δx in the case of the single-beam method. This would be explained by elongation of the beam profile [34]. A broadened beam profile increases the signal correlation coefficient ρ_s and decreases the phase shift noise.

The phase shift noise against the $ESNR$ is shown in Fig.6. To virtually change the $ESNR$, complex circular Gaussian noise is numerically generated and added to complex OCT data. The phase shift noise decreases as the $ESNR$ increases. However, the phase shift noise approaches an asymptotic value.

In the high- $ESNR$ regime, decorrelation phase shift noise is dominant. The equivalent representative SNR of a signal correlation coefficient $ESNR_{\rho_s}$ can be described by equating $\rho_s = 1/(1 + ESNR_{\rho_s}^{-1})$ as

$$ESNR_{\rho_s} = \frac{\rho_s}{1 - \rho_s}. \quad (39)$$

When the $ESNR$ is larger than this $ESNR_{\rho_s}$, the $ESNR$ is no longer a dominant limitation of phase noise but the signal correlation ρ_s is. In the case of the current dual-beam system, the $ESNR_{\rho_s}|_{\rho_s=\rho_{\text{Pol.}}} \approx 10.6$ dB and phase shift noise approaches $\sigma_{\Delta\phi}|_{\rho=\rho_{\text{Pol.}}} \approx 0.63$ radians in the high- $ESNR$ regime.

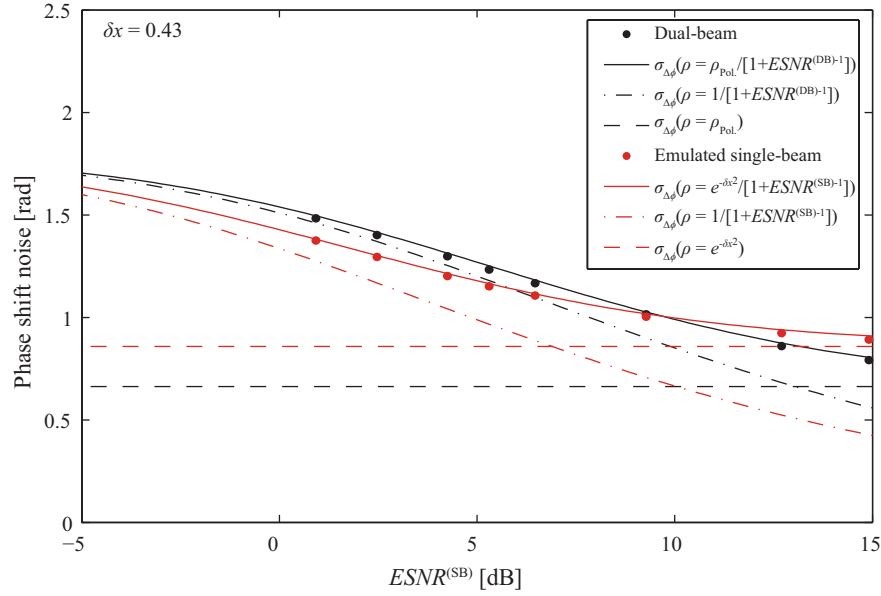


Fig. 6. Phase shift noises vs $ESNR$.

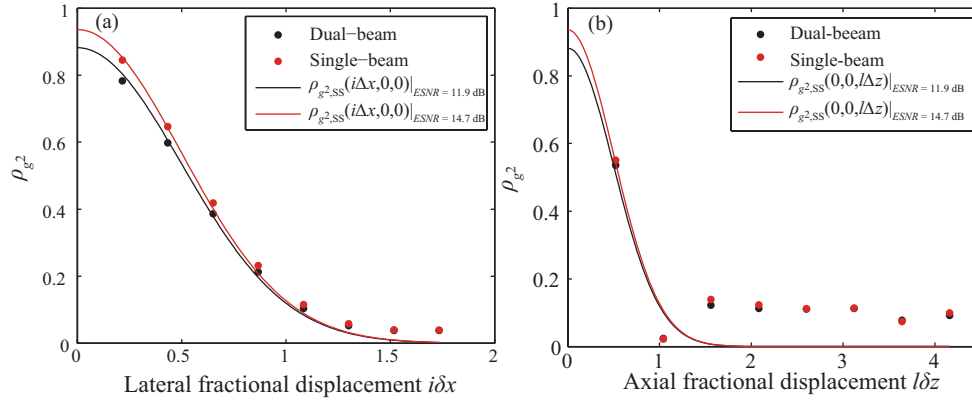


Fig. 7. Profiles of the correlation coefficients of the Hermitian products with displacement along (a) the lateral direction and (b) the axial direction. In each figure, the horizontal axis is fractional displacement $i\delta x = i\Delta x/w$ and $l\delta z = l\Delta z/\zeta$, where i and l are the displacements in the number of pixels along lateral and axial directions, respectively. $\delta x = 0.22$ and $\delta z = 0.52$. Solid curves are the expected correlation coefficients from Eq. (29).

4.2.1. Averaged phase shift noise

In practical applications, spatial complex averaging (Eq. (26)) is used to enhance the contrast of phase-resolved images. The performances with averaging in conventional and dual-beam-scan phase-resolved flow imaging are compared in this section.

First, estimations of the correlation coefficient of the Hermitian product ρ_{g^2} are evaluated because ρ_{g^2} is essential to the estimation of the effective number of independent samples $ENIS$ (Eq. (27)). The Hermitian product $g_1^*g_2$ was calculated for the single B-scan image and the

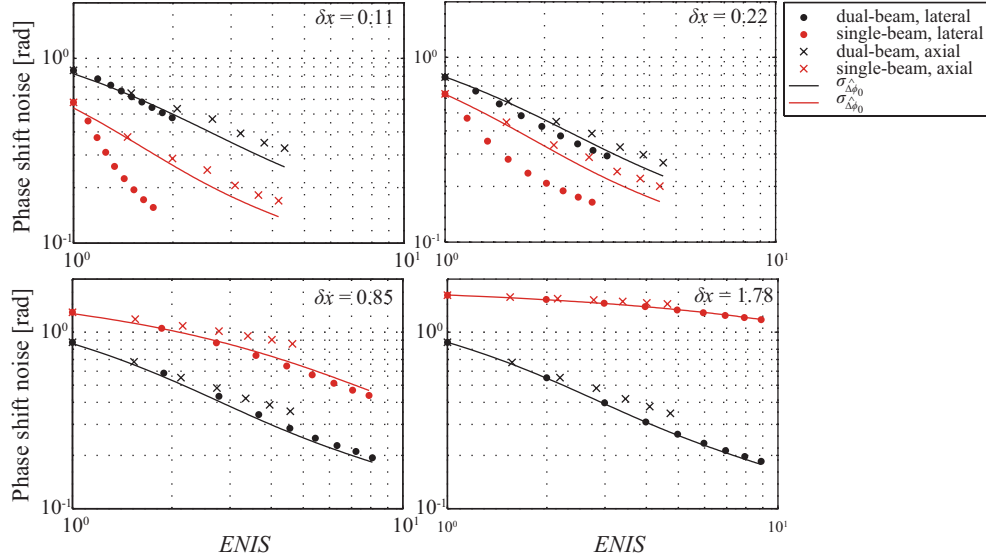


Fig. 8. Phase shift noise vs effective number of independent samples.

spatial autocorrelation was obtained in the ROI according to the spatial displacement steps Δx and Δz , which correspond to the spatial lengths according to the single pixel. Figure 7 shows the profiles of estimated $\rho_{g^2,SS}$. The horizontal axis of each plot is normalized by the beam spot radius, $w = 16.5 \mu\text{m}$, and the axial resolution defined as half width at e^{-2} of axial PSF, $\zeta = 4/\Delta k = 9.5 \mu\text{m}/\sqrt{2 \log 2} = 8.1 \mu\text{m}$. The solid curves in each plot show the expected profiles from Eqs. (29) by substituting $\rho_{s,SS}^{(DB)} = \rho_{\text{Pol}}$ and $\rho_{s,SS}^{(SB)} = e^{-\delta x^2}$. Here, ρ_{Pol} and the $ENIS$ were calculated from data obtained in the experiment. They show that the experimental data and estimation using Eq. (29) are in good agreement.

The suppression of phase shift noise by the moving average is shown in Fig. 8. The effective number of independent samples within the window $ENIS$ is calculated using Eq. (27). Solid curves show the approximate phase shift noise numerically simulated using Eqs. (25), (43), and (44) by summing series up to the 50-th order. The experimental results and numerical estimations are in good agreement for large δx .

When the fractional sampling step is very small, (i.e., $\delta x < 0.2$), measured results with lateral averaging deviate from predicted values. Perhaps under this condition, the OCT signals do not significantly differ between the two axial lines. The phase shift estimation $\sigma_{\Delta \hat{\phi}_0}$ does not obey Eq. (24). When correlation coefficient ρ_s is close to 1, phase shift $\Delta \phi_0$ is constant. In addition, if δx is small, the Hermitian products extracted along the lateral direction can be considered as a sum of a constant phasor and a random phasor. If this assumption is valid, the phase shift noise will decrease by the square root of the number of averaged realizations. In fact, the noise suppression ratio under this condition is close to $\frac{1}{\sqrt{N}}$, where N is the number of sampling points in the lateral averaging window.

In order to compare dual-beam and single-beam methods, phase shift noise with lateral moving average was calculated where the window size is up to the optical resolution. The window

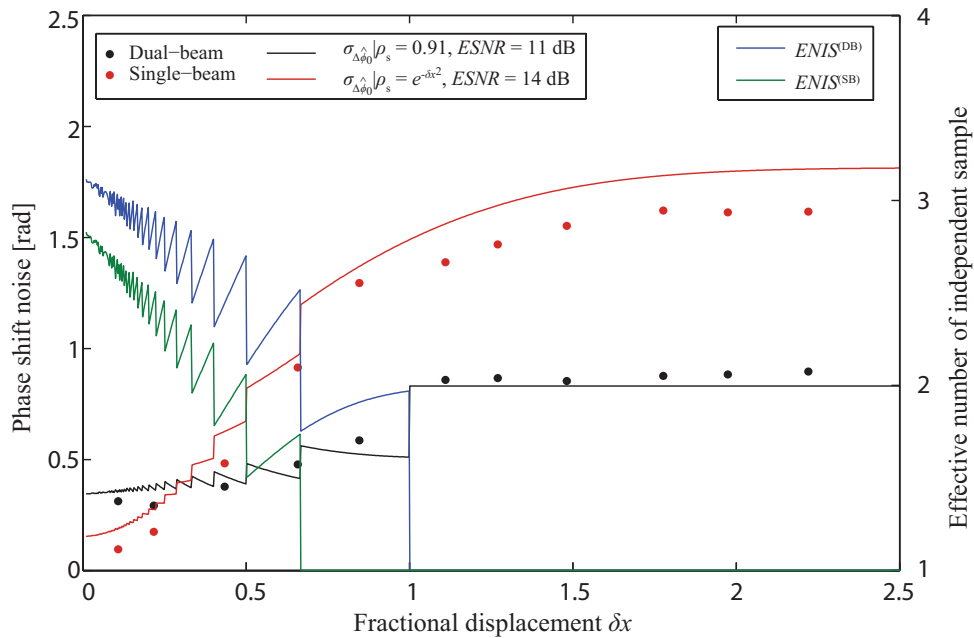


Fig. 9. Phase shift noise vs fractional sampling step with averaging using a constant window size.

sizes for each method are as follows.

$$I^{(DB)} = \begin{cases} \lfloor \frac{2}{\delta x} \rfloor & \frac{2}{\delta x} \geq 1, \\ 1 & \text{otherwise} \end{cases} \quad (40)$$

$$I^{(SB)} = \begin{cases} \lfloor \frac{2}{\delta x} \rfloor - 1 & \frac{2}{\delta x} \geq 2, \\ 1 & \text{otherwise.} \end{cases} \quad (41)$$

These phase shift noises and corresponding $ENIS$ s calculated from Eqs. (27), (40), and (41) are plotted in Fig.9. Since the window size must be an integers (Eqs. (40) and (41)), the population standard deviation of the MLE of phase shift $\sigma_{\Delta\phi_0}$ and estimated effective number $ENIS$ exhibit discontinuous values along δx as shown by solid curves in Fig.9. The transitional point of the fractional sampling step is nearly the same as that without averaging. However, the phase shift noise of the dual-beam method at small fractional sampling step is reduced and approaches that of the single-beam method.

5. Discussions

The essential factor that explains the phase shift noise in phase-resolved OCT is the correlation coefficient of measured OCT signals. The phase shift noise relying on the SNR can be treated as the decorrelation of measured signals caused by additive noise. Hence, the phase shift noises derived from additive noise and structural decorrelation are unified. The presented statistical model accounts for the spatial variation of the instantaneous SNR; i.e., speckle. The introduced statistics well describe the imaging performance of phase-resolved OCT.

In the formulation of the correlation coefficient of OCT signals (Eq. (14)), we did not consider an effect of displacement of objects during integration of photons at a detector [24]. This

effect will result in changes of population parameters in the presented statistical model; i.e., $\Delta\phi_0$ and ρ_s . The further alterations for the presented study according to the previous work will provide a statistical analysis tool of phase-resolved OCT that is more accurate.

In this study, we compared the dual-beam Doppler method and the inter-line single-beam Doppler method. When the transversal sampling is coarse, the phase shift noise of the dual-beam method is less than that of the conventional Doppler method as expected. This indicates that there is a great advantage in the case of systems with high spatial resolution. The imaging speed and/or imaging range can be increased by increasing the transversal sampling step as a level of phase shift noise is low.

Recently, Doppler methods with dedicated scanning protocols have been employed to increase the time delay and increase the flow sensitivity [35–37]. With high-dense transversal sampling, it is predicted that the single-beam method will surpass the dual-beam method. However, repeatability of a beam scanning mechanism and/or sample fluctuation perhaps limit the advantage [37]. As shown in Fig.3, a small reduction of the correlation coefficient will result in a rapid increase of the phase shift noise. On the other hand, the dual-beam-scan method can be used with a simple raster scanning protocol.

For vasculature imaging in optical coherence angiography, squared Doppler phase shifts are calculated to contrast vessels [4]. The response to flow can be defined by the second moment of the phase shift estimation $E[\Delta\hat{\phi}^2]$. Since the lateral motion of samples reduces the correlation coefficient between OCT signals at different time points and hence increases $E[\Delta\hat{\phi}^2]$, the squared Doppler phase shift imaging is expected to be sensitive to not only axial motion but also lateral movement.

6. Conclusion

The statistical properties of phase-resolved OCT imaging were described. The investigated statistics of phase-resolved OCT were validated by evaluating phase shift noise measured with a static tissue phantom. Flow imaging performances of dual-beam-scan phase-resolved Doppler OCT and the conventional single-beam method were compared and discussed using the presented statistics. The dual-beam method exhibited lower phase shift noise for coarse transversal sampling than the single-beam method. The presented statistics of phase-resolved OCT are useful in investigating, comparing, and designing phase-resolved OCT systems.

Appendix A. Moments of the maximum likelihood estimate of phase shift

From the moment generating function, the n -th order moment of the sample phase shift is obtained as

$$E[\Delta\hat{\phi}_0^n] = (-1)^{n/2} \frac{\pi^n \cos(\frac{n\pi}{2})}{n+1} + 2 \sum_{l=1}^{\infty} \left\{ \frac{(-1)^l \rho^l \Gamma(\frac{l}{2}+1) \Gamma(\frac{l}{2}+\nu) {}_2F_1(\frac{l}{2}, \frac{l}{2}-\nu+1; l+1; \rho^2)}{\pi \Gamma(\nu) \Gamma(l+1)} \times \left[\frac{\partial^n}{\partial s^n} \frac{\sinh(\pi s) [s \cos(l\Delta\phi_0) - l \sin(l\Delta\phi_0)]}{l^2 + s^2} \right] \Big|_{s \rightarrow 0} \right\}. \quad (42)$$

The first and second moments are then obtained by setting n as 1 and 2 in Eq. (42):

$$E[\Delta\hat{\phi}_0] = - \sum_{l=1}^{\infty} \frac{2(-\rho)^l \sin(l\Delta\phi_0) \Gamma(\frac{l}{2}+1) \Gamma(\frac{l}{2}+\nu) {}_2F_1[\frac{l}{2}, \frac{l}{2}-\nu+1; l+1; \rho^2]}{l \Gamma(\nu) \Gamma(l+1)}, \quad (43)$$

$$E \left[\Delta \hat{\phi}_0^2 \right] = \frac{\pi^2}{3} + \sum_{l=1}^{\infty} \frac{4(-\rho)^l \cos(l\Delta\phi_0) \Gamma(\frac{l}{2} + 1) \Gamma(\frac{l}{2} + \nu) {}_2F_1[\frac{l}{2}, \frac{l}{2} - \nu + 1; l + 1; \rho^2]}{l^2 \Gamma(\nu) \Gamma(l + 1)}. \quad (44)$$